

Bioinspired 1D Superparamagnetic Magnetite Arrays with Magnetic Field Perception

Xiangyu Jiang, Jiangan Feng, Lei Huang, Yuchen Wu, Bin Su, Wensheng Yang,*
Liqiang Mai,* and Lei Jiang*

Magneto-sensitivity is a ubiquitous ability for many organism species, which can perceive Earth's magnetic field for orientation and navigation purposes, including homing, building activities, and long-distance migration.^[1–5] Although the biophysical mechanisms underlying these geomagnetic-perception behaviors are elusive, many magnetic crystals of biomineralization magnetites (Fe_3O_4) have been extracted from the body of different organisms, such as the homing pigeon (*Columbia livia*),^[6] magnetotactic bacterium (*Magnetospirillum magneticum*),^[7] sockeye salmon (*Oncorhynchus nerka*),^[8] and bumblebees (*Bombus terrestris*).^[9] For perception of geomagnetic fields, the organism possesses two mechanisms: (1) Single-domain magnetites exist in magnetotactic bacterium and sockeye salmon. (2) Superparamagnetic magnetite exists in pigeon and migratory birds. In these two mechanisms, superparamagnetic magnetite appears in an organism as 1D arrays such as the upper beak skin tissue of pigeons.^[10–12]

Inspired by the magnetosensing behaviors in nature, artificial magnetic-field perception could possibly be achieved by fabricating a kind of micro-/nanoscale assembled by superparamagnetic magnetite nanoparticles, which requires synthesis of nanoparticles and fabrication of anisotropic-magnetization structures. Recent advances in colloidal chemistry have provided many potential protocols for synthesis of superparamagnetic-magnetite nanoparticles with controlled sizes and morphologies,^[13–15] thus the key challenges for realizing

bioinspired magnetic-field perception are focused on large-scale assembly of magnetite nanoparticles into ordered assemblies with anisotropic magnetization. Generally, these magnetite nanoparticles can be fabricated into ordered assemblies by applying a magnetic field, yielding ordered alignment of nanoparticles along the magnetic field.^[16,17] However, these assembled nanoparticles have limited magnetization anisotropy due to the low aspect ratio of the prepared micro-/nanoscale arrays, especially the 1D arrays. To improve the anisotropy, some micro-/nanoprocessing methods, such as light/electron-beam lithography,^[18] focused ion beam lithography^[19] and templating techniques,^[20] can be employed to assemble nanoparticles into high-aspect-ratio patterns with designable geometric parameters. However, these top-down processing techniques are restricted by low efficiency and high cost. Compared to the top-down techniques, bottom-up assembly methods, such as inkjet printing, soft lithography, and nanoimprinting, possess many advantages of high efficiency, low cost, and large-scale processability.^[21–24] Yet owing to the uncontrollable dewetting process of liquid in these methods, the fabricated micro-/nanoscale structures often display disordered particle stacking and high-density defects, inducing the deteriorated performance of assemblies.

To assemble nanoparticles into 1D arrays, herein, we propose and experimentally demonstrate a bottom-up liquid-processing method, termed capillary-bridge-mediated assembly (CBMA), allowing the fission of continuous aqueous thin-film dispersion of magnetite and formation of individual microscaled capillary bridges with 1D configuration and high aspect ratio. With the evaporation of water, the stacking of magnetite nanoparticles generates several millimeters long, submicrometer wide wires with ultrahigh aspect ratio >5000 , strict alignment and precise position. A micropillar-structured template with regionally different wettability is employed: the superhydrophobic sidewalls and gaps of micropillars modified with heptadecafluorodecyltrimethoxysilane (FAS) create an air cushion to support the thin-film liquid, whereas the hydrophilic tops of micropillars act as high-adhesion sites to guide the fission of liquid and anchor the capillary bridge. Here, solvothermal synthesized polycrystalline magnetite nanoparticles (Fe_3O_4 -NPs) were selected due to their room-temperature superparamagnetism, uniform size, and good dispersibility in water. By in situ observation of dewetting process of a fluorescently labeled aqueous dispersion of magnetites under a dark-field fluorescence microscope, the mechanism of CBMA method was revealed by displaying a continuous process: a thin-film dispersion is sandwiched between micropillars and desired flat substrate followed by fission of liquid and formation of microscaled individual capillary bridges, which finally generates magnetite nanoparticle arrays.

Dr. X. Y. Jiang, Prof. W. S. Yang, Prof. L. Jiang
State Key Laboratory of Supermolecular Structure
and Materials

College of Chemistry

Jilin University

Changchun 130012, P. R. China

E-mail: wsyang@jlu.edu.cn; jianglei@iccas.ac.cn

Dr. J. G. Feng, Dr. Y. C. Wu, Prof. L. Jiang

Laboratory of Bioinspired Smart Interfacial Science

Technical Institute of Physics and Chemistry

Chinese Academy of Sciences

Beijing 100190, P. R. China

Mr. L. Huang, Prof. L. Q. Mai

State Key Laboratory of Advanced Technology for Materials

Synthesis and Processing

Wuhan University of Technology

Wuhan 430070, China

E-mail: mlq518@whut.edu.cn

Dr. B. Su

Department of Chemical Engineering

Monash University

Clayton, Victoria 3800, Australia



DOI: 10.1002/adma.201601609

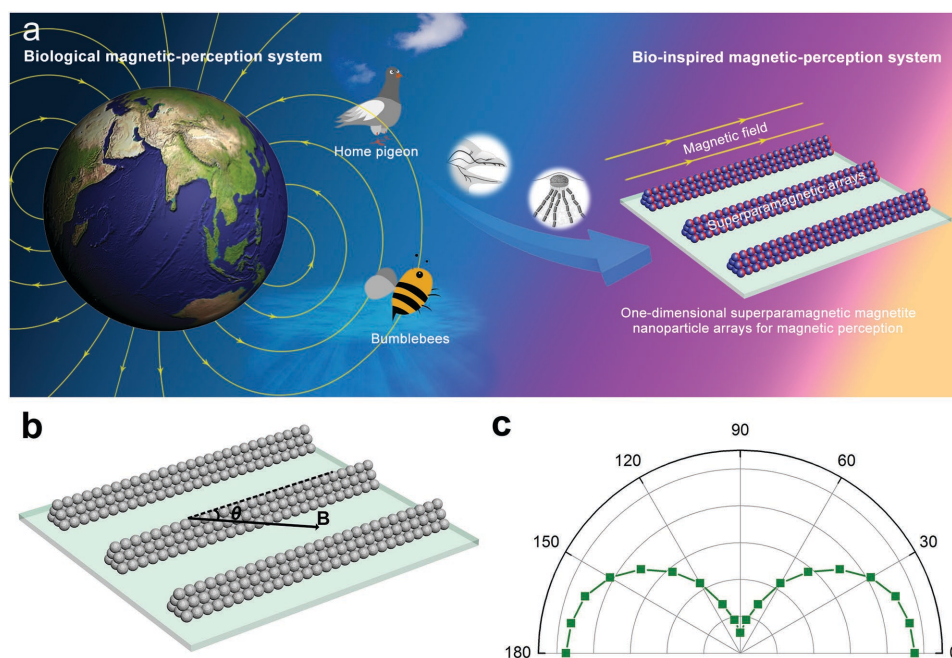


Figure 1. Bioinspired artificial magnetic-perception system. a) Drawing showing a biological magnetic-perception system (left), in which many organism species, such as home pigeon, bumblebees, detect the Earth's magnetic field through biomineralization superparamagnetic magnetite assemblies in cells, especially the upper beak skin cell in home pigeon and our bioinspired artificial magnetic-perception system (right) depend on the 1D superparamagnetic magnetite nanoparticle arrays with anisotropic magnetization to achieve the magnetic perception. b) Schematic illustration of 1D Fe₃O₄-NP assemblies. The magnetic-perception ability was measured by changing the direction of magnetic field, θ . c) A typical curve illustrates the dependence of magnetization of 1D Fe₃O₄-NP arrays on the θ .

Additionally, these high-aspect-ratio 1D arrays show highly anisotropic magnetization under a rotating magnetic field, thus proof-of-principle demonstrating their application as bioinspired magnetic-field-perception system.

For biological magnetic-perception system in nature, the magnetosensitivity originates from the magnetic-sensitive cells, which contain biomineralization superparamagnetic magnetite assemblies, yielding successful signal transformation from magnetic orientation and intensity to neural response (Figure 1a, left). This 1D arrays reflected in the pigeon beak skin is more obvious the nanocrystals with sizes of several nanometers aggregate nanoparticles with the size of a few hundred nanometers then these nanoparticles assemble into 1D arrays.^[10] Inspired by this mechanism in biological system, we propose an artificial biomimetic magnetic-perception system, which is constructed by alignment of superparamagnetic Fe₃O₄-NPs in one dimension. The magnetic-perception ability of the artificial system can be explained by the coalescence of superparamagnetism and 1D architecture: the nonpermanent magnetic moment in superparamagnetic crystals can track the axis of ambient magnetic field rapidly, meanwhile, the high-aspect-ratio 1D architecture yields anisotropic integrated magnetization intensity when the included angle (θ) between the axis of 1D assemblies and the direction of magnetic field was altered (Figure 1b). The maximum magnetization emerges when the direction of magnetic field is parallel to the axis of 1D arrays, whereas achieves minimum value at the perpendicular direction (Figure 1c). This angle-dependence magnetization will generate sensitivity to ambient magnetic field.

To realize the bioinspired artificial magnetic perception, first, we synthesized polycrystalline Fe₃O₄-NPs by solvothermal method as described in the previous report.^[25] To confirm the morphology and magnetic properties of Fe₃O₄-NPs, we performed scanning electron microscopy (SEM) and magnetic characterization. A uniform diameter of ≈ 150 nm can be observed from SEM image (Figure S1a, Supporting Information). We also find the Fe₃O₄-NPs is composed of nanocrystals with sizes of ≈ 5 nm, which is the provenance of the superparamagnetic. Magnetization curve displays nearly no hysteresis of these particle, demonstrating the superparamagnetic nature of Fe₃O₄-NPs (Figure S1b, Supporting Information). Due to the citrate groups anchored on the surface introduced during the synthesis process, the Fe₃O₄-NPs shows excellent dispersibility in water, which is benefit to the subsequent assembly process.

After synthesis and characterization of Fe₃O₄-NPs, we performed the CBMA experiment by harnessing a micropillar-structured template with height of 20 μm , width of 2 μm and separation of 5 μm . The micropillar-structured template was processed by light lithography followed by reactive-ion etching (see details in Experimental Section). The micropillars were modified into regionally different wettability before performing the CBMA experiment. To modify the micropillars' sidewalls and gaps with low surface energy, the tops of micropillars were protected followed by FAS modification and the protection layer was removed finally (see details in Experimental Section; see schematic illustration in Figure S3, Supporting Information). To confirm the successful FAS modification, we performed Raman mapping at both sidewall and top regions of micropillar. High-intensity

Raman signals of FAS in sidewall and gap regions is displayed as yellow and pink color, whereas blue color emerge at top regions, illustrating that FAS molecules are mainly distributed at sidewall and gap regions of template (Figure S4, Supporting Information). High water contact angle of 150° is achieved on the FAS-modified micropillar-structured template, which is attributed to the air cushion anchored by nonwetable micropillars' gaps (Figure S5a, Supporting Information). Meanwhile, the modified template also shows high adhesion and the water drop can hang on its surface, which indicates the hydrophilic nature of micropillars' tops (Figure S5b, Supporting Information).

To perform the CBMA experiment, Fe_3O_4 -NP dispersion was sandwiched between the micropillars' tops and flat target substrate, generating a continuous thin-film liquid with controlled thickness of $\approx 5 \mu\text{m}$ (see details in Experimental Section). To reveal the assembly mechanism of 1D Fe_3O_4 -NP arrays, a red fluorescence dye rhodamine B was doped the dispersion of magnetite nanoparticles followed by observing the time-sequence dewetting process of assembly system under fluorescence microscope. At the preliminary stage, a sandwich-structure assembly system of "target substrate thin-film dispersion-micropillar template" can be observed under microscope (Figure 2d). Owing to the hydrophobicity of the gap and sidewall regions, the dispersion film can be lifted by air cushion in the gaps of micropillars, as illustrated in Figure 2a.

With the gradually decreased quantity of water in evaporation process, the continuous liquid film begins to dewetting,

Distinguished from thin-film liquid between two planer substrate, the dewetting process of liquid in our CBMA system is restricted by the micropillar substrate. The gas-liquid-solid triphase contact line (TCL) on hydrophilic micropillars' tops is anchored, inducing the fission of continuous film into multiple individual capillary bridges pinned on micropillars. As schematically illustrated in Figure 2b and shown in Figure 2e, capillary bridges form on each micropillar accompanied with the restriction of Fe_3O_4 -NPs in these several micrometers wide and several millimeter long assembly systems. According to the previously study on capillary bridges, the fission of liquid film in our system is mainly caused by Laplace pressure,^[26–28] which value can be expressed by the following equation:

$$P_{\text{Laplace}} = \gamma/R \quad (1)$$

where γ is the surface tension of our dispersion and R is the curvature radius of liquid film between two micropillars (Figure 2g). With the gradual dewetting of water between two micropillars, the curvature radius R decreases until achieve a critical value and triggers the fission of liquid film. Further dewetting will incur the shrinkage of liquid bridges, inducing higher aspect ratio as well as more precise position and strict alignment of Fe_3O_4 -NP assemblies (Figure 2h). After the totally evaporation of water, the Fe_3O_4 -NP arrays generate on the target substrate (Figure 2c,f).

To characterize the morphologies, crystal properties of assembled 1D Fe_3O_4 -NP arrays, we performed SEM, powder

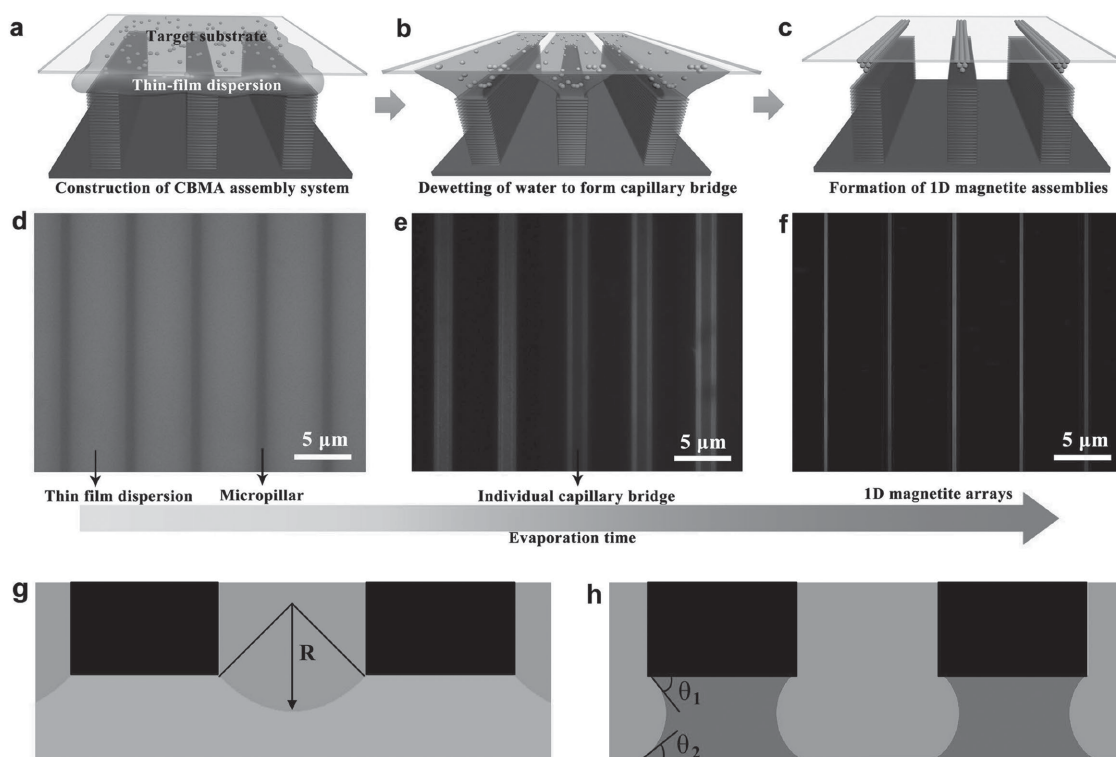


Figure 2. Assembly mechanism of 1D magnetite arrays revealed by time-sequence fluorescence microscope images. a–c) Schematic drawing of CBMA method for assembly of 1D magnetite arrays. d–f) Time-sequence fluorescence microscope images illustrate a process: construction of sandwiched "target substrate-thin film dispersion-micropillar template" assembly system, guided fission of liquid film to generate individual capillary bridges and yielding of 1D magnetite arrays. g) Schematic illustration of liquid film restricted between micropillars' tops and flat substrate with a curvature radius R . h) Capillary bridges anchored on the micropillars' tops after fission of liquid film.

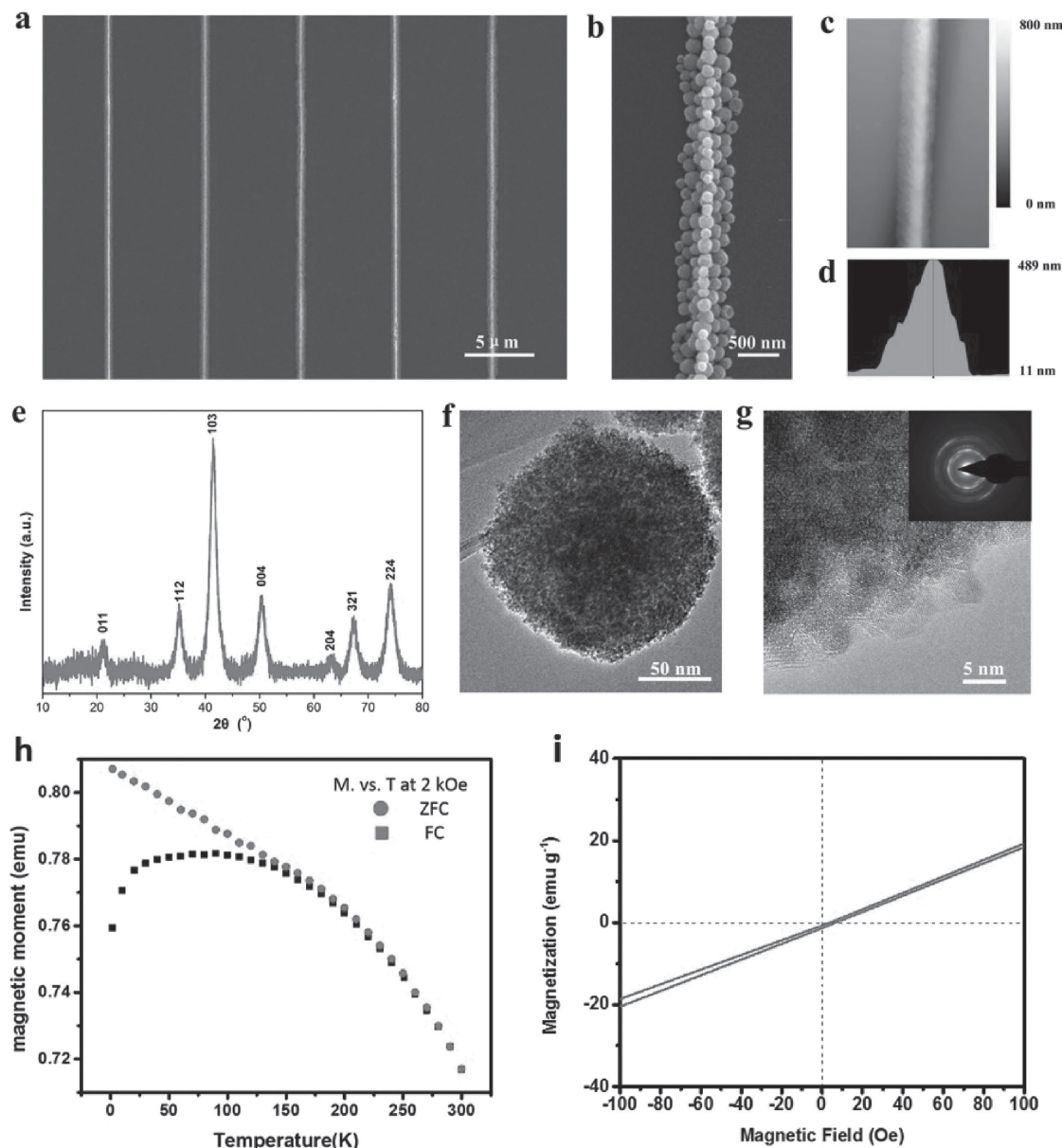


Figure 3. Morphology and crystal-structure characterizations and size tuning of 1D Fe_3O_4 -NP assemblies. a) SEM image of 1D Fe_3O_4 -NP arrays. b) Zoom-in SEM image, c) AFM image, and d) height diagram of a single 1D Fe_3O_4 -NP assembly. e) PXRD pattern of Fe_3O_4 nanoparticles corresponding to a typical magnetite structure (JCPDS No. 19-629). f) TEM image of Fe_3O_4 nanoparticle in our experiment. g) Zoom-in TEM image showing a polycrystalline pomegranate-like configuration of Fe_3O_4 nanoparticle. Inset is the SAED pattern of Fe_3O_4 nanoparticle, indicating the polycrystalline nature of the particle. h) Dependence of magnetization on temperature for field cooled (F.C) under 2 kOe applied field and zero field cooled (Z.F.C) nanoparticle of Fe_3O_4 i) Magnetization curve of Fe_3O_4 nanoparticles indicating the superparamagnetic nature.

X-ray diffraction (PXRD), transmission electron microscopy (TEM), selected area electron diffraction (SAED), and atomic force microscopy (AFM). SEM image shown in **Figure 3a** depicts strictly aligned (misalignment angle of $<1^\circ$), precisely positioned (controlled distance of $\approx 6 \mu\text{m}$) and high-aspect-ratio (>5000) 1D Fe_3O_4 -NP arrays. Zoom-in SEM image (Figure 3b) displays that the Fe_3O_4 NPs are stacked into a volcano-like shape with straight boundary, ordered packing and uniform width of 550 nm. A height of 489 nm is observed by AFM (Figure 3c). The height diagram also depicts the volcano-like packing of this

Fe_3O_4 -NP assembly (Figure 3d). The crystal structure of Fe_3O_4 nanoparticles is determined by PXRD (Figure 3e), showing diffraction peaks of 21.2° , 35.2° , 41.4° , 50.4° , 63.4° , 67.3° , and 74.1° , which can be assigned to the (011), (112), (103), (004), (204), (321), and (224) lattice planes of magnetite-structured Fe_3O_4 (JCPDS No. 19-629). Low-magnification TEM image of a single Fe_3O_4 nanoparticle (Figure 3f) shows that the diameter is about 150 nm and composed by many secondary clusters, which is the provenance of the superparamagnetic. The SAED pattern of a single Fe_3O_4 nanoparticle (Figure 3g, inset)

confirms the polycrystalline characteristic of nanoparticle. A high-resolution TEM image reveals that these secondary clusters are nanocrystals with sizes of ≈ 5 nm (Figure 3g). We performed the low-temperature magnetic measurement (saturation field after zero-field cooling (ZFC) and field-cooling (FC) treatments, the strength of the magnetic field of 2kOe). The temperature changed from 2 K to 300 K. The weight of the test sample was 10 mg. The result shows that the ZFC and FC curves are branching, which means the nanoparticles may show superparamagnetism (Figure 3h). To confirm the superparamagnetism, we obtained a magnetization curve showing enlarged hysteresis loop (-100 Oe to 100 Oe). The

remanence and coercivity is almost zero (Figure 3i). AC susceptibility under different frequencies between 2 and 300 K is shown in Figure S6 (Supporting Information).

To tune the sizes of 1D Fe_3O_4 -NP assemblies, we performed the CBMA experiments by using the Fe_3O_4 dispersion with different mass ratios of nanoparticles. A single-line chain of Fe_3O_4 nanoparticles can be generated at the mass ratio of 2 mg mL^{-1} with width of ≈ 150 nm (Figure 4a). With the increasing mass ratios, the Fe_3O_4 nanoparticles can be stacked into 1D assemblies with different widths and layers. 1D Fe_3O_4 -NP assemblies with widths of 310 and 820 nm can be fabricated at the concentration of 5 and 15 mg mL^{-1} , respectively (Figure 4b,c). As Figure 3k

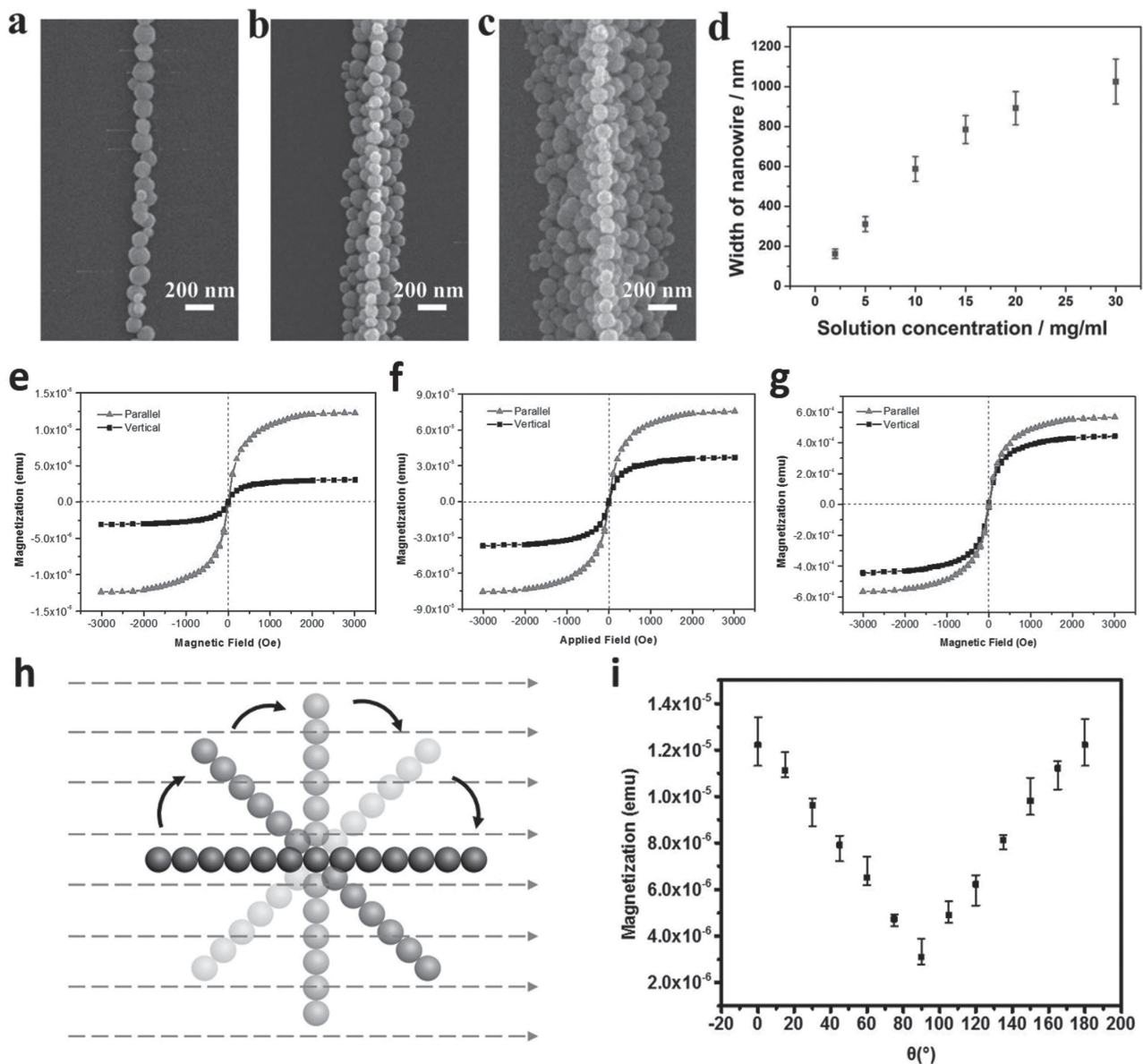


Figure 4. Anisotropic magnetic property of 1D Fe_3O_4 -NP arrays. a–c) 1D Fe_3O_4 -NP arrays with width of $\approx 0.16 \mu\text{m}$, $\approx 0.31 \mu\text{m}$, and $\approx 0.82 \mu\text{m}$ fabricated by dispersions with nanoparticle mass ratios of 2, 5, 15 mg mL^{-1} . d) The dependence of width of 1D Fe_3O_4 -NP arrays on the mass ratio of nanoparticles. e–g) Magnetic properties of 1D Fe_3O_4 -NP arrays with width of $\approx 0.16 \mu\text{m}$, $\approx 0.31 \mu\text{m}$, and $\approx 0.82 \mu\text{m}$. Lower width induces high aspect ratio, thus yielding larger anisotropy of magnetization. h) Schematic drawing of 1D Fe_3O_4 -NP arrays in the magnetic field. i) The curve illustrates the dependence of magnetization of 1D Fe_3O_4 -NP arrays on the θ .

shows, the widths of 1D assemblies can be tailored from 160 to 1060 nm by varying mass ratios of 2 to 30 mg mL⁻¹ (Figure 4d).

To evaluate the anisotropic magnetic properties, we measured the magnetization curves of 1D Fe₃O₄-NP arrays at room temperature. As shown in Figure 4e–g, all 1D Fe₃O₄-NP arrays with different widths display superparamagnetic nature and anisotropic magnetization owing to the high-aspect-ratio structures. This anisotropic magnetization phenomenon originates from the superparamagnetism of these Fe₃O₄ nanoparticles, when magnetic particles are small enough that, in addition to containing but one domain, the magnetization of these assembled particles can be sufficiently equilibrated by the thermal vibration, inducing the nonpermanent magnetic moment under zero applied magnetic field.^[29–31] In our experiment, the superparamagnetic property of Fe₃O₄ NPs is initiated by the sub-10 nm clusters in a polycrystalline particle. Although these particles exhibit no magnetization under zero applied magnetic field, the magnetization of individual magnetic domains have long-range order. These magnetic moments can be aligned under an applied magnetic field and the magnetization intensity is determined by the integrated magnetic moments along the magnetic field direction, **B**. According to the magnetization curves in Figure 4e–g, the magnetization intensity achieves maximum value (M_{\max}) when the direction of **B** is parallel to the axis of 1D Fe₃O₄-NP arrays, whereas that has minimum value (M_{\min}) when the direction of **B** is orthogonal with the axis of 1D arrays. The value of M_{\max}/M_{\min} can be employed to evaluate the magnetic anisotropy of the 1D arrays and determined as 4.02, 2.06, and 1.29 for 1D arrays with widths of 0.16, 0.31, and 0.82 μm , respectively. For the fabricated 1D Fe₃O₄-NP arrays, their length is determined by length of micropillars and keeps as ≈ 2 μm . Therefore, larger width will induce lower aspect ratio and lower magnetization anisotropy (Figure 4g). This anisotropic magnetization characteristic of 1D Fe₃O₄-NP arrays can provide an effective approach to magnetic-perception applications. The schematic drawing of 1D Fe₃O₄-NP arrays rotate in a fixed magnetic field (Figure 4h), therefore we determined that the curve illustrates the dependence of magnetization of 1D Fe₃O₄-NP arrays on θ . The maximum of the magnetic induction intensity is the parallel direction, the minimum is the vertical direction (Figure 4i).

In summary, we have fabricated a bioinspired 1D Fe₃O₄-NP array with high aspect ratio, strict alignment and precise position through employing a micropillar-structured template with asymmetric wettability. Through investigating the dewetting process, capillary bridges with 1D configuration has been demonstrated for guiding the assembly behavior of Fe₃O₄ NPs. Owing to the superparamagnetic nature of Fe₃O₄ NPs and high-aspect-ratio characteristic of 1D arrays, these assembled structures have been demonstrated with highly anisotropic magnetization, which possess the ability of bioinspired magnetic field perception. The magnetic anisotropy can be manipulated by tuning the aspect ratio of 1D structures with changing widths of structures. It is anticipated that such findings not only facilitate the fundamental understanding and applications of anisotropic superparamagnetic structures for magnetic field perception, but also provide a facile and effective approach for fabricating high-aspect-ratio 1D assemblies for other implementations, such as electronic devices, biosensing, and biometric techniques.

Experimental Section

Fabrication of Micropillar-Structured Templates: To fabricate the micropillar structures, light lithography was processed on nitrogen doped, <100> oriented silicon wafers by using a direct laser-writing apparatus (Heidelberg DWL200), which can transfer the computer-predefined patterns onto the photoresist (Shipley Microposit S1800 series)-coated wafer. The patterns of photoresist formed after irradiation, followed by deep reactive-ion etching with fluorine-based reagents for 6 min. The geometry of micropillars can be conveniently designed by tuning the parameters of patterns. After resist stripping (Microposit Remover 1165), the substrates were cleaned using ethanol and acetone.

Selected Modification of Micropillars into Top Hydrophilic and Sidewall Hydrophobic State: To modify micropillars' sidewalls into hydrophobic state, a 10 μL droplet of SU-8 photoresist liquid was spin-coated onto a flat substrate, yielding a SU-8 thin layer. Subsequently, a micropillar-structured template was contacted with the SU-8 loading substrate for ≈ 3 min at room temperature followed by peeling off the sticky flat substrate. Then, the SU-8 layer coated on the micropillars' tops was exposed to the UV irradiation for ≈ 1 min. After the protection of top regions, the hydrophobic modification was performed by loading heptadecafluorodecyltrimethoxysilane (FAS) in a decompression environment at room temperature for 24 h and then heated at 80 $^{\circ}\text{C}$ for 3 h. Finally, the SU-8 layers were removed and the top-hydrophilic, sidewall & gap-hydrophobic micropillar-structured template was generated.

Fabrication of 1D Fe₃O₄-NP Assemblies by CBMA Method: A flat glass coverslip, a ≈ 10 μL droplet of Fe₃O₄-NP dispersion, and a micropillar-structured template with selected modification were combined into a sandwiched configuration. This assembly system was kept at temperature of 25 $^{\circ}\text{C}$ and humidity of 60% to control the dewetting in a mild environment. After ≈ 8 h evaporation of water, 1D Fe₃O₄-NP arrays were generated upon the flat glass coverslip.

Characterizations: Field-emission scanning electron microscopy (FE-SEM, Hitachi, S-4800, Japan) was employed at an accelerating voltage of 5.0 kV to characterize the morphologies of Fe₃O₄ nanoparticles, micropillar-structured template, and 1D Fe₃O₄-NP arrays. To determine the height of 1D Fe₃O₄-NP assemblies, atomic force microscopy (AFM) image was collected using Bruker MultiMode 8 Atomic Force Microscope. The crystal phase of nanoparticles was characterized by powder X-ray diffraction (PXRD) on a Rigaku D/MAX-III diffractometer with monochromatized Mo K α radiation ($\lambda = 0.7093$ \AA). The crystal structure of Fe₃O₄ nanoparticles was investigated using a JEOL TEM-2100 operating at a 200 kV accelerating voltage. Magnetic property measurement was carried out on a superconducting quantum interference device (SQUID, Quantum Design MPMS-7). The ZFC&FC curves were obtained from physical property measurement system (SQUID, Quantum Design PPMS).

Supporting Information

Supporting Information is available from the Wiley Online Library or from the author.

Acknowledgements

X.Y. Jiang and J.G. Feng contributed equally to this work. The authors thank the National Natural Science Foundation (21201169) and Australian Research Council's Discovery Early Career Researcher Award (DECRA) funding scheme (DE140100541) for financial support.

Received: March 24, 2016

Revised: April 21, 2016

Published online:

- [1] M. M. Walker, C. E. Diebel, C. V. Haugh, P. M. Pankhurst, J. C. Montgomery, C. R. Green, *Nature* **1997**, 390, 371.
- [2] W. Wiltschko, J. Traudt, O. Gunturkun, H. Prior, R. Wiltschko, *Nature* **2002**, 419, 467.
- [3] K. J. Lohmann, C. M. F. Lohmann, N. F. Putman, *J. Exp. Biol.* **2007**, 210, 3697.
- [4] K. J. Lohmann, *Nature* **2010**, 464, 1140.
- [5] R. J. Gegear, L. E. Foley, A. Casselman, S. M. Reppert, *Nature* **2010**, 463, 804.
- [6] G. Falkenberg, G. Fleissner, K. Schuchardt, M. Kuehbacher, P. Thalau, H. Mouritsen, D. Heyers, G. Wellenreuther, G. Fleissner, *PLoS One* **2010**, 5, e9231.
- [7] M. I. Siponen, P. Legrand, M. Widdrat, S. R. Jones, W.-J. Zhang, M. C. Y. Chang, D. Faivre, P. Arnoux, D. Pignol, *Nature* **2013**, 502, 681.
- [8] J. L. Kirschvink, *Nature* **1997**, 390, 339.
- [9] P. Jandacka, B. Kasparova, Y. Jiraskova, K. Dedkova, K. Mamulova-Kutlakova, J. Kukutschova, *Biometals* **2015**, 28, 89.
- [10] G. Fleissner, E. H. Rotzler, M. Hanzlik, M. Winklhofer, G. Fleissner, N. Petersen, W. Wiltschko, *J. Comp. Neurol.* **2003**, 458, 350.
- [11] M. Hanzlik, C. Heunemann, E. Holtkamp-Rotzler, M. Winklhofer, N. Petersen, G. Fleissner, *Biometals* **2000**, 13, 325.
- [12] L. Tian, B. Xiao, W. Lin, S. Zhang, R. Zhu, Y. Pan, *Biometals* **2007**, 20, 197.
- [13] S. Sun, H. Zeng, *J. Am. Chem. Soc.* **2002**, 124, 8204.
- [14] A. Bharde, A. Wani, Y. Shouche, P. A. Joy, B. L. V. Prasad, M. Sastry, *J. Am. Chem. Soc.* **2005**, 127, 9326.
- [15] U. Jeong, X. Teng, Y. Wang, H. Yang, Y. Xia, *Adv. Mater.* **2007**, 19, 33.
- [16] M. B. Bannwarth, S. Utech, S. Ebert, D. A. Weitz, D. Crespy, K. Landfester, *ACS Nano* **2015**, 9, 2720.
- [17] R. Sheparovych, Y. Sahoo, M. Motornov, S. Wang, H. Luo, P. N. Prasad, I. Sokolov, S. Minko, *Chem. Mater.* **2006**, 18, 591.
- [18] E. M. Hicks, S. Zou, G. C. Schatz, K. G. Spears, R. P. Van Duyne, L. Gunnarsson, T. Rindzevicius, B. Kasemo, M. Käll, *Nano Lett.* **2005**, 5, 1065.
- [19] P. Peinado, S. Sangiao, J. M. De Teresa, *ACS Nano* **2015**, 9, 6139.
- [20] S. Siavoshi, C. Yilmaz, S. Somu, T. Musacchio, J. R. Upponi, V. P. Torchilin, A. Busnaina, *Langmuir* **2011**, 27, 7301.
- [21] T. Kraus, D. Brodoceanu, N. Pazos-Perez, A. Fery, *Adv. Funct. Mater.* **2013**, 23, 4529.
- [22] H. Kang, R. Kitsomboonloha, J. Jang, V. Subramanian, *Adv. Mater.* **2012**, 24, 3065.
- [23] J. Zhang, B. Yang, *Adv. Funct. Mater.* **2010**, 20, 3411.
- [24] I. Park, S. H. Ko, H. Pan, C. P. Grigoropoulos, A. P. Pisano, J. M. J. Fréchet, E. S. Lee, J. H. Jeong, *Adv. Mater.* **2008**, 20, 489.
- [25] J. Liu, Z. Sun, Y. Deng, Y. Zou, C. Li, X. Guo, L. Xiong, Y. Gao, F. Li, D. Zhao, *Angew. Chem. Int. Ed.* **2009**, 48, 5875.
- [26] P. P. Bhat, S. Appathurai, M. T. Harris, M. Pasquali, G. H. McKinley, O. A. Basaran, *Nat. Phys.* **2010**, 6, 625.
- [27] E. J. De Souza, M. Brinkmann, C. Mohrdieck, E. Arzt, *Langmuir* **2008**, 24, 8813.
- [28] D. J. Broesch, F. Dutka, J. Frechette, *Langmuir* **2013**, 29, 15558.
- [29] C. P. Bean, *J. Appl. Phys.* **1955**, 26, 1381.
- [30] J. I. Gittleman, B. Abeles, S. Bozowski, *Phys. Rev. B* **1974**, 9, 3891.
- [31] M. Mikhaylova, D. K. Kim, N. Bobrysheva, M. Osmolowsky, V. Semenov, T. Tsakalakos, M. Muhammed, *Langmuir* **2004**, 20, 2472.